Clustering-based redshift estimation: application to VIPERS/CFHTLS

V. Scottez,[1][★] Y. Mellier,[1,2] B. R. Granett,[3] T. Moutard,[4] M. Kilbinger,[1,2]
M. Scodeggio,[5] B. Garilli,[5] M. Bolzonella,[6] S. de la Torre,[4] L. Guzzo,[3] U. Abbas,[7]
C. Adami,[4] S. Arnouts,[4] D. Bottini,[5] E. Branchini,[8,9,10] A. Cappi,[6,11] O. Cucciati,[12,6]
I. Davidzon,[4,6] A. Fritz,[5] P. Franzetti,[5] A. Iovino,[3] J. Krywult,[13] V. Le Brun,[4]
O. Le Fèvre,[4] D. Maccagni,[5] K. Małek,[14] F. Marulli,[12,15,6] M. Polletta,[5] A. Pollo,[16,14]
L. A. M. Tasca,[4] R. Tojeiro,[17] D. Vergani,[18,6] A. Zanichelli,[19] J. Bel,[20] J. Coupon,[21]
G. De Lucia,[22] O. Ilbert,[4] H. J. McCracken[1] and L. Moscardini[6,12,15]

[1]*Institut d'Astrophysique de Paris, UMR7095 CNRS, Université Pierre and Marie Curie, 98 bis boulevard Arago, F-75014 Paris, France*
[2]*CEA/Irfu/SAp Saclay, Laboratoire AIM, F-91191 Gif-sur-Yvette, France*
[3]*INAF – Osservatorio Astronomico di Brera, Via Brera 28, 20122 Milano, via E. Bianchi 46, I-23807 Merate, Italy*
[4]*Aix Marseille Université, CNRS, LAM (Laboratoire d'Astrophysique de Marseille) UMR 7326, F-13388 Marseille, France*
[5]*INAF – Istituto di Astrofisica Spaziale e Fisica Cosmica Milano, via Bassini 15, I-20133 Milano, Italy*
[6]*INAF – Osservatorio Astronomico di Bologna, via Ranzani 1, I-40127, Bologna, Italy*
[7]*INAF – Osservatorio Astronomico di Torino, I-10025 Pino Torinese, Italy*
[8]*Dipartimento di Matematica e Fisica, Università degli Studi Roma Tre, via della Vasca Navale 84, I-00146 Roma, Italy*
[9]*INFN, Sezione di Roma Tre, via della Vasca Navale 84, I-00146 Roma, Italy*
[10]*INAF – Osservatorio Astronomico di Roma, via Frascati 33, I-00040 Monte Porzio Catone (RM), Italy*
[11]*Laboratoire Lagrange, UMR7293, Université de Nice Sophia Antipolis, CNRS, Observatoire de la Côte d'Azur, F-06300 Nice, France*
[12]*Dipartimento di Fisica e Astronomia – Alma Mater Studiorum Università di Bologna, viale Berti Pichat 6/2, I-40127 Bologna, Italy*
[13]*Institute of Physics, Jan Kochanowski University, ul. Swietokrzyska 15, PL-25-406 Kielce, Poland*
[14]*National Centre for Nuclear Research, ul. Hoza 69, PL-00-681 Warszawa, Poland*
[15]*INFN, Sezione di Bologna, viale Berti Pichat 6/2, I-40127 Bologna, Italy*
[16]*Astronomical Observatory of the Jagiellonian University, Orla 171, PL-30-001 Cracow, Poland*
[17]*Institute of Cosmology and Gravitation, Dennis Sciama Building, University of Portsmouth, Burnaby Road, Portsmouth PO1 3FX, UK*
[18]*INAF – Istituto di Astrofisica Spaziale e Fisica Cosmica Bologna, via Gobetti 101, I-40129 Bologna, Italy*
[19]*INAF – Istituto di Radioastronomia, via Gobetti 101, I-40129 Bologna, Italy*
[20]*Aix Marseille Université, CNRS, CPT, UMR 7332, F-13288 Marseille, France*
[21]*Astronomical Observatory of the University of Geneva, ch. d'Ecogia 16, CH-1290 Versoix, Switzerland*
[22]*INAF – Osservatorio Astronomico di Trieste, via G. B. Tiepolo 11, I-34143 Trieste, Italy*

ABSTRACT

We explore the accuracy of the clustering-based redshift estimation proposed by Ménard et al. when applied to VIMOS Public Extragalactic Redshift Survey (VIPERS) and Canada–France–Hawaii Telescope Legacy Survey (CFHTLS) real data. This method enables us to reconstruct redshift distributions from measurement of the angular clustering of objects using a set of secure spectroscopic redshifts. We use state-of-the-art spectroscopic measurements with $i_{AB} < 22.5$ from the VIPERS as reference population to infer the redshift distribution of galaxies from the CFHTLS T0007 release. VIPERS provides a nearly representative sample to a flux limit of $i_{AB} < 22.5$ at a redshift of >0.5 which allows us to test the accuracy of the clustering-based redshift distributions. We show that this method enables us to reproduce the true mean colour–redshift relation when both populations have the same magnitude limit. We also show that this technique allows the inference of redshift distributions for a population fainter than the reference and we give an estimate of the colour–redshift mapping in this case. This last point is of great interest for future large-redshift surveys which require a complete faint spectroscopic sample.

Key words: methods: data analysis – surveys – clustering – galaxies: distances and redshifts.

[★] E-mail: scottez@iap.fr

1 INTRODUCTION

Large future redshift surveys like the ESA *Euclid space mission* (Laureijs et al. 2011; Amendola et al. 2013) aim to probe dark energy with unprecedented accuracy. Many of the cosmological measurements to be performed with these surveys – e.g. tomographic weak lensing, tomographic clustering – will require extremely well-characterized redshift distributions (Albrecht et al. 2006; Huterer et al. 2006; Ma, Hu & Huterer 2006; Thomas et al. 2011).

Since it is impractical to measure spectroscopic redshifts for hundreds of millions of galaxies – especially extremely faint ones – these experiments are largely dependent upon photometric redshifts: i.e. estimates of the redshifts of objects based only on flux information obtained through broad-band filters. Photos-z also require large spectroscopic samples both for the calibration of empirical methods (Connolly et al. 1995) and the building of representative template libraries for template-fitting techniques (Coleman et al. 1980). However, current and future spectroscopic surveys will be highly incomplete due to selection biases dependent on redshift and galaxy properties (Cooper et al. 2006). Because of this, along with the catastrophic photometric errors that can occur at a significant (~ 1 per cent) rate (Sun et al. 2009; Bernstein & Huterer 2010), photometric redshifts are not sufficiently precise. If future dark energy experiments have to reach their goals, it is necessary to develop a method to infer, at least, the redshift distribution with high precision.

Current projections for cosmic shear measurements estimate that the true mean redshift of objects in each photo-z bin must be known to better than $\sim 0.002(1 + z)$ (Knox, Song & Zhan 2006; Zhan 2006; Zhan & Knox 2006) with stringent requirements on the fraction of unconstrained catastrophic outliers (Hearin et al. 2010) while the width of the bin must be known to $\sim 0.003(1 + z)$. Newman et al. (2015) investigated the spectroscopic needs for dark energy imaging experiments and insisted on the extremely high (~ 99.9 per cent) completeness required for calibration techniques.

The idea of measuring redshift distributions using the apparent clustering of objects on the sky is not new. It was first developed by Seldner & Peebles (1979), Phillipps & Shanks (1987) and Landy, Szalay & Koo (1996). This was practically forgotten mainly due to the rise of photometric redshifts. To face the challenges of future and ongoing dark energy imaging experiments, Newman (2008), Matthews & Newman (2010) and Matthews & Newman (2012) re-applied this method on simulations, while McQuinn & White (2013) proposed an optimal estimator for such a measurement. In this paper, we explore the clustering-based redshift estimation, i.e cluster-z, via a local (i.e. within few Mpc) approach introduced by Ménard et al. (2013, hereafter M13), validated with simulations by Schmidt et al. (2013) and compared to spectroscopic redshift at limiting magnitude $r_{\rm model} < 19$ by Rahman et al. (2015, hereafter R15). Recently, Schmidt et al. (2015) applied this technique to continuous fields by inferring the redshift distribution of the cosmic infrared background while Rahman et al. (2016a) and Rahman et al. (2016b) explored this method in near-infrared using Two Micron All Sky Survey Extended and Point Source Catalogues as well as the Sloan Digital Sky Survey Photometric Galaxies. This work aims to explore the strength of cluster-z at fainter magnitude $i_{\rm AB} < 22.5$ using real data similar to what will be available with *Euclid* in term of filters and observational strategy and demonstrate our ability to recover the redshift distribution of an unknown sample with $22.5 < i_{\rm AB} < 23$ when the reference sample used for calibration has only $i_{\rm AB} < 22.5$.

This paper is organized as follows. In Section 2, we review the clustering-based redshift formalism, while the data used in this work

are described in Section 3. Then in Section 4, we show our ability to measure the clustering redshift distribution using a tomographic photo-z approach. We also show that this method allows the estimation of redshift distribution when the sample of unknown redshift is fainter than the reference one. Finally, we free cluster-z from the use of photo-z in Section 5 by selecting subsamples in colour-space and we explore in this case the reconstruction of the colour–redshift mapping for faint objects. Conclusions are presented in Section 6.

2 CLUSTERING-BASED REDSHIFT: FORMALISM

The method used in this paper is based on the work of M13 and R15. We refer the reader to those papers for more details. In this section, we briefly review the formalism.

The key point is that correlated galaxies are at the same location in redshift and on the sky. Sources at different redshift are uncorrelated. This clustering information is encoded into the two-point correlation function as an excess probability – compared to a random distribution – to find two objects close together. This is valid in 3D and, by projection, on the sky. Using a reference sample of secure spectroscopic redshifts – and by looking at the galaxy cluster scale – it is then possible to extract the excess probability of finding a population of galaxies at a given redshift. Obviously, the reference population and the unknown one – for which angular positions are known but redshifts are not – have to overlap on the sky.

The mean surface density of unknown objects at a distance θ from a reference one which is at a redshift z, is

$$\Sigma_{\rm ur}(\theta, z) = \Sigma_{\rm R}[1 + \omega_{\rm ur}(\theta, z)], \tag{1}$$

where $\Sigma_{\rm R}$ is the random surface density of the unknown sample and $\omega_{\rm ur}(\theta, z)$ is the two-point angular cross-correlation function between the two samples. Then, one can define the integrated cross-correlation function as

$$\bar{\omega}_{\rm ur}(z) = \int_{\theta_{\rm min}}^{\theta_{\rm max}} {\rm d}\theta \, W(\theta) \, \omega_{\rm ur}(\theta, z), \tag{2}$$

where the range covered by θ varies with redshift and corresponds to physical distances from few hundred kiloparsecs to several megaparsecs. Here we worked within a [0.2, 6] Mpc annulus. $W(\theta)$ is a weight function – $\propto \theta^{-0.8}$ – aimed at optimising the overall S/N and whose integral is normalized to unity. This integrated cross-correlation function represents the excess probability, with respect to a Poisson distribution, to find an object of the unknown sample at an angular distance between $\theta_{\rm min}$ and $\theta_{\rm max}$ from a generic object of the reference sample at redshift z.

One can also write this quantity as a function of the redshift selection function of sample $i \in \{u, r\}$, ${\rm d}N_i/{\rm d}z$, as well as the galaxy-dark matter biases, $\bar{b}_i(z)$, and the dark matter correlation function, $\bar{\omega}_{\rm m}(z)$:

$$\bar{\omega}_{\rm ur} = \int {\rm d}z' \, \frac{{\rm d}N_{\rm u}}{{\rm d}z}(z') \, \frac{{\rm d}N_{\rm r}}{{\rm d}z}(z') \, \bar{b}_{\rm u}(z') \, \bar{b}_{\rm r}(z') \, \bar{\omega}_{\rm m}(z'). \tag{3}$$

Applying the narrow sample approximation for the reference sample ${\rm d}N_{\rm r}/{\rm d}z = N_{\rm r}\delta_{\rm D}(z' - z)$ – with $\delta_{\rm D}$ the Dirac delta function – we can then simply invert the previous integral and obtain:

$$\frac{{\rm d}N_{\rm u}}{{\rm d}z}(z) \propto \bar{\omega}_{\rm ur}(z) \times \frac{1}{\bar{b}_{\rm u}(z)} \times \frac{1}{\bar{b}_{\rm r}(z)\bar{\omega}_{\rm m}(z)}, \tag{4}$$

where $\bar{\omega}_{\rm ur}(z)$ can be directly measured in data, $\bar{b}_{\rm r}(z)$ can be measured in the reference sample, $\bar{\omega}_{\rm m}(z)$ is given by the cosmology and $\bar{b}_{\rm u}(z)$ is the only unknown quantity.

Considering a narrow redshift distribution for the unknown sample, we can neglect the variation of its galaxy-dark matter bias with respect to the variation of the number of objects:

$$\frac{d \log \ dN_u/dz}{dz} \gg \frac{d \log \ \bar{b}_u}{dz}, \tag{5}$$

we obtain:

$$\frac{dN_u}{dz}(z) \propto \bar{\omega}_{ur}(z) \left(\frac{1}{\bar{b}_r(z) \ \bar{\omega}_m(z)} \right). \tag{6}$$

As in equation (5), we can neglect the redshift variation of $\sqrt{\bar{\omega}_m}$ with respect to dN_r/dz:

$$\frac{d \log \ dN_r/dz}{dz} \gg \frac{d \log \ \sqrt{\bar{\omega}_m}}{dz}. \tag{7}$$

Thus, introducing the clustering amplitude of the reference sample, $\beta_r(z)$, we can write:

$$\beta_r(z) = \sqrt{\frac{\bar{\omega}_{rr}(z)}{\bar{\omega}_{rr}(z_0)}} \propto \frac{\bar{b}_r(z)}{\bar{b}_r(z_0)}. \tag{8}$$

Note that we can define $\beta_u(z)$ in the same way. As explained in R15, one should note that this quantity is different from the linear galaxy bias which is usually defined only on large scales for which the galaxy and dark matter density fields are, on average, linearly related. This bias definition includes contributions from small scales where the galaxy and matter fields are non-linearly related. We can then rewrite a model-independent version of equation (6) and we obtain:

$$\frac{dN_u}{dz}(z) \propto \bar{\omega}_{ur}(z)/\beta_r(z). \tag{9}$$

Finally, the redshift distribution is normalized to the number of objects in the unknown sample through

$$\int dz \ dN_u/dz = N_u. \tag{10}$$

It is important to realize that to be able to write and use equation (9), we have to select unknown samples with relatively small redshift distributions to have $\bar{b}_u(z)$ or $\beta_u(z)$ slowly varying with redshift. The ability of selecting subsamples with narrow redshift distributions is quite important to consider: $d\beta_u/dz = 0$.

To directly measure the integrated cross-correlation function, we can simply use the Davis & Peebles (1983) estimator:

$$\bar{\omega}_{ur}(z) = \frac{\langle \Sigma_{ur} \rangle_z}{\Sigma_R} - 1. \tag{11}$$

The error in the measurement is then estimated through Poisson statistic and is given by

$$\sigma_{\bar{\omega}}^2 = \left(\frac{\bar{\omega}+1}{\sqrt{N_{ur}}} \right)^2 + \left(\frac{\bar{\omega}+1}{\sqrt{N_R}} \right)^2, \tag{12}$$

where N_{ur} is the neighbours number of unknown objects over $[\theta_{min}, \theta_{max}]$ around reference galaxies and N_R is the corresponding number of neighbours for a random distribution.
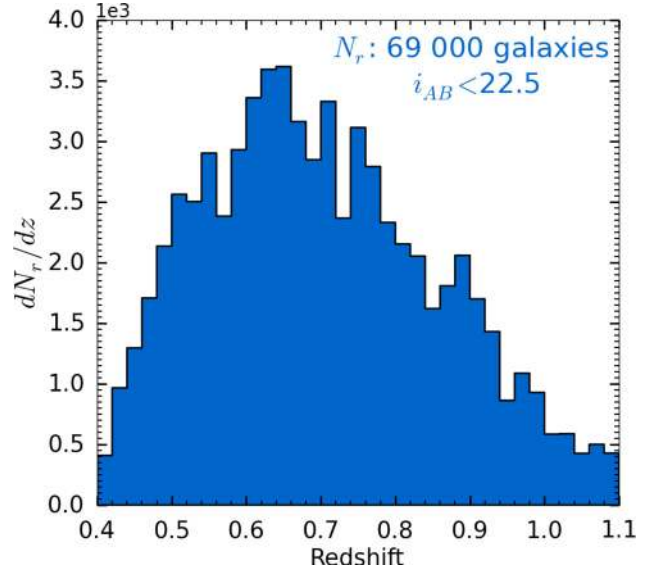
Figure 1. The redshift distribution of the reference sample built from VIPERS data with $i_{AB} < 22.5$ and assuming a bin width $\delta z = 0.02$.

3 DATA ANALYSIS

3.1 The data sets

3.1.1 VIPERS: reference sample

The VIMOS Public Extragalactic Redshift Survey (VIPERS;[1] Guzzo et al. 2014) is an ongoing spectroscopic survey whose aim is to map the detailed spatial distribution of galaxies. The survey is made of two distinct fields inside the Canada–France–Hawaii Telescope Legacy Survey (CFHTLS) W1 and W4 fields. The total survey area is 24 deg². VIPERS spectra are the results of 440h of observation at the Very Large Telescope (VLT) in Chile. Galaxies were selected to have $z > 0.4$ using the following colour criteria:

$$(r - i) > 0.5(u - g) \ \ \text{OR} \ \ (r - i) > 0.7. \tag{13}$$

The 1σ random error in the measured VIPERS redshift is: $\sigma_z = 0.00047(1 + z)$.

Our reference sample is made from a selection of VIPERS objects in two separate fields, W1 and W4, outside CFHTLS masks and with secure spectroscopic redshifts ($CL > 95$ per cent) corresponding to flags: 2, 3, 4 and 9 inside the redshift range [0.4, 1.1]. The resulting reference sample is composed of $N_r \sim 69\,000$ galaxies with $i_{AB} < 22.5$ over an area of $\sim$24 deg². It corresponds to the reference population used in all the analysis presented in this paper. Its redshift distribution is shown in Fig. 1.

3.1.2 CFHTLS: unknown sample

The CFHTLS²-Wide includes four fields labelled W1, W2, W3 and W4. Complete documentation of the CFHTLS-T0007 release can be found at the Canada–France–Hawaii Telescope (CFHT)³ site. In summary, the CFHTLS-Wide is a five-band survey of intermediate depth. It consists of 171 MegaCam deep pointings (of 1 deg² each)

which, as a consequence of overlaps, consists of a total of ~155 deg^2 in four independent contiguous patches, reaching a 80 per cent completeness limit in AB of $u^* = 25.2$, $g = 25.5$, $r = 25.0$, $i = 24.8$, $z = 23.9$ for point sources.

In this work, we focused on the W1 and W4 fields in common with VIPERS and used the magnitudes from the VIPERS Multi-Lambda Survey (Moutard et al. 2016a) which is based on the CFHTLS-T0007 photometry. We selected all galaxies in the same region of the sky covered by VIPERS and which are outside CFHTLS masks resulting in a sample of ~570 000 galaxies over ~24 deg^2. Since we use a sample of VIPERS galaxies in the redshift range $0.4 < z < 1.1$, we will not be able to measure any signal outside this interval. Unknown objects outside this range will bias the overall redshift distribution, since it is normalized to the total number of unknown galaxies following equation (10). To reduce this problem, we selected objects with a photometric redshift matching the range [0.5, 1] in redshift. Considering the number of photometric sources at the edges and the photometric redshift accuracy, we can expect to have less than 1 per cent of objects outside the redshift range covered by the reference sample. The resulting population corresponds to the parent unknown sample. This parent sample is then divided into two samples: a bright sample with $i_{AB} < 22.5$ chosen to match the magnitude limit of the reference population from VIPERS; and a faint sample whose galaxies have magnitudes $22.5 < i_{AB} < 23$. These are the samples for which we recover the redshift distributions in this paper.

3.1.3 Reference clustering amplitude measurement

As previously seen in Section 2, the determination of a clustering redshift distribution requires the knowledge of the evolution with redshift of the clustering amplitude of the reference population, $\beta_r(z)$. This quantity can be directly measured using equation (8) and is shown in Fig. 2. We also show a smoothed version obtained by convolving the binned measurements with a Hann filter of width $\Delta z = 0.02$. Since we are only interested in the relative variation of $\beta_r(z)$ – see equations (9) and (10) – we chose to normalize this
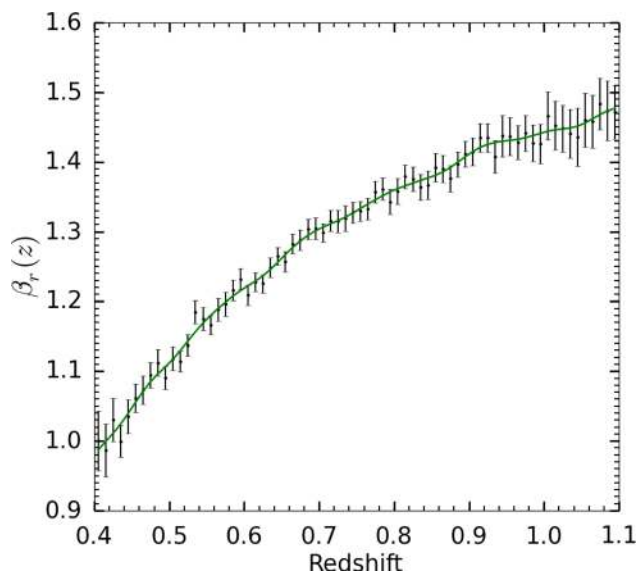
Figure 2. Clustering amplitude evolution of the reference sample normalized to 1 at $z_0 = 0.4$. The solid line is the smoothed version used in this paper.

quantity to unity at $z_0 = 0.4$. This figure shows an increase of ~40 per cent of the clustering amplitude between redshift 0.5 and 1.1 which is in agreement with the analysis performed by Marulli et al. (2013).

4 TOMOGRAPHIC SAMPLING

As seen in Section 2, reducing the variation of $\beta_u(z)$ is a key point of this method. In this section, we aim at demonstrating our ability to measure the redshift distribution. To reduce the variation of $\beta_u(z)$, we choose to work with tomographic subsamples of the unknown population. One can then consider: $d\beta_u/dz = 0$, for each of these subsamples. The tomography is done by selecting objects using their photometric redshifts based on the marginalization over the redshift of all the models (Z_{ML} in Lephare).

4.1 Photometric redshifts estimation

The photometric redshifts used in this paper come from the VIPERS-MLS and are described in Moutard et al. (2016a). The photometry combines optical data from the CFHTLS-T0007 with near-infrared data (limited at $Ks_{AB} < 22$). The authors have used ISO magnitudes that provide the best estimate of galaxy colour and corrected them for a mean difference between ISO and AUTO magnitudes (over the g, r, i and Ks bands). This was done in order to recover a good approximation of the galaxy total flux while keeping the best determination of the galaxy colours. In our case, this recalibration is important since it leads to a smoother surface density fluctuation from tile to tile.

4.2 Magnitude limit for both samples: $i < 22.5$

We selected objects with $i_{AB} < 22.5$ in the unknown population. The resulting sample contains $N_u \sim 203\,000$ galaxies.

We split them into 68 tomographic subsamples of 3000 objects each. Thus, we measure the integrated cross-correlation from few kpcs to several Mpcs in reference slices of width $\delta z = 0.02$.

Fig. 3 shows the recovered clustering redshift distribution for a particular tomographic bin selected using the photometric redshift. We also show the redshift distribution obtained when using photo-z Probability Distribution Functions (PDFs). This PDF is obtained by stacking individual PDFs defined as a Gaussian: $G(z_{phot}, \sigma = z_{phot,max} - z_{phot,min})$, where $z_{phot,min/max}$ are the 1σ lower/upper limit, respectively. This plot shows the ability of reconstructing the redshift distribution with the clustering method. Recovered distributions (black dots) are significantly narrower that the photo-z PDF (dashed green) and consistent with the distribution of spectroscopic VIPERS galaxies (in blue) selected on their photometric redshift to match the selected tomographic bin.

Note that this is not a rigorous comparison since the spectroscopic sources show in blue are not exactly the same objects considered in the unknown sample. Moreover, since there are only few objects in this distribution, one can only compare the statistical properties which are expected to be similar. All distributions are normalized to unity.

In the same way, we measured the clustering redshifts distributions for all the 68 tomographic subsamples. The results of these $68 \times 35 = 2\,380$ measurements of $\bar{\omega}_{ur}$ are translated into redshift distributions following equation (9).

In Fig. 4, each vertical line corresponds to a clustering redshift distribution measured in a tomographic sample of mean photometric redshift $\bar{z}_{phot}$ similar to the one shown in Fig. 3. Fig. 4 shows
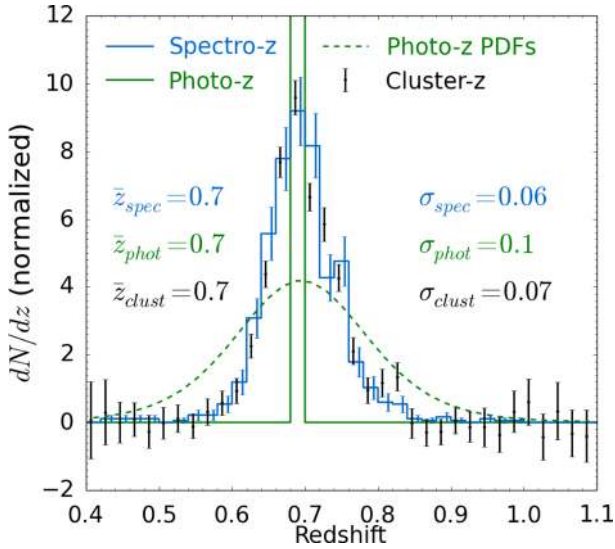
Figure 3. Example of the cluster-z distribution (black) obtained from equation (9) for a tomographic sample selected using the photo-z (green line). The dashed green line shows the redshift distribution obtained when summing the photo-z PDFs. The blue line shows the spectroscopic redshift distribution with Poisson error bar of the VIPERS sources selected using their photometric redshifts to match the tomographic bin.

the corresponding redshift distributions in the (z_{clust}; z_{phot}) plane and illustrates the global agreement between cluster and photo-z. Negative values correspond to stochastic density fluctuations and are not statistically significant.

To compare these two measurements in a more quantitative way, we compute the accuracy of the estimate of the mean redshift of a distribution as: $\sigma = \sigma_{\Delta \bar{z}}/(1 + \bar{z}_{\mathrm{spec}})$, where $\Delta \bar{z} = |\bar{z}_{\mathrm{clust/phot}} - \bar{z}_{\mathrm{spec}}|$ is the difference between the mean clustering redshift and the mean spectroscopic redshift of a distribution.

We use the normalized median absolute deviation to estimate the accuracy as previously defined:

$$\sigma_{\Delta \bar{z}} = 1.48 \times \mathrm{median}(|\bar{z}_{\mathrm{clust/phot}} - \bar{z}_{\mathrm{spec}}|), \qquad (14)$$

where the mean redshifts are computed as

$$\bar{z} = \frac{1}{\sum \mathrm{d}N/\mathrm{d}z} \left(\sum_i z_i \frac{\mathrm{d}N_i}{\mathrm{d}z} \right). \qquad (15)$$

For each cluster-z distribution, we show on the top panel of Fig. 5 the difference $\bar{z}_{\mathrm{clust/phot}} - \bar{z}_{\mathrm{spec}}$. We see that cluster-z and photo-z are in relatively good agreement. This figure demonstrates the ability of cluster-z to infer redshift distributions of a sample for which photometric redshifts are known and can be used to reduce the variation of $\beta_{\mathrm{u}}(z)$ by selected subsamples localized in redshift.
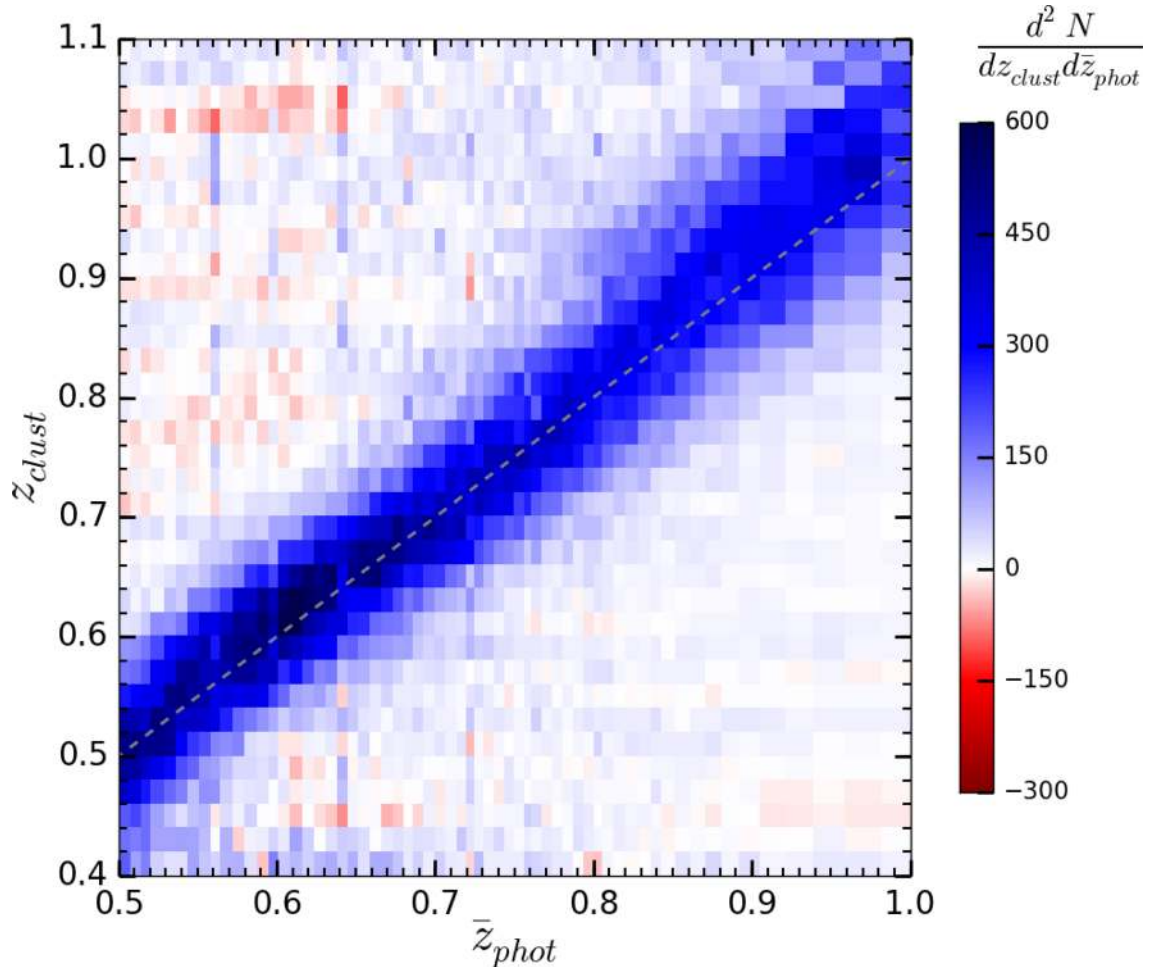
Figure 4. Density map showing the 2380 clustering measurements made in Section 4.2. Each vertical line corresponds to a clustering redshift distribution measured in a tomographic sample of mean photometric redshift $\bar{z}_{\mathrm{phot}}$. Each column is normalized to match the number of unknown objects.
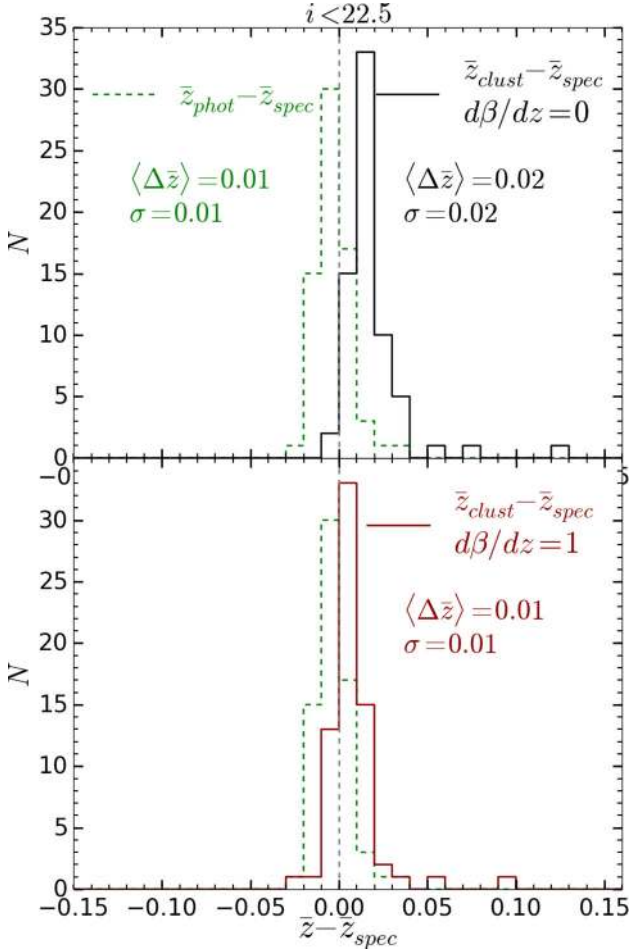
Figure 5. Top panel: histograms showing the distribution of the difference between the mean of the clustering/photometric redshift distribution and the mean of the spectroscopic redshift distribution: $\bar{z}_{\mathrm{clust/phot}} - \bar{z}_{\mathrm{spec}}$(black and dashed green lines, respectively). Cluster-z measurements were made considering $\mathrm{d}\beta_{\mathrm{u}}/\mathrm{d}z = 0$. Bottom panel: same quantities as in the top panel but the cluster-z measurements were performed considering a linear evolution for the clustering amplitude of the unknown population: $\mathrm{d}\beta_{\mathrm{u}}/\mathrm{d}z = 1$.

The lower panel shows the $\bar{z}_{\mathrm{clust/phot}} - \bar{z}_{\mathrm{spec}}$ residuals when considering a linear evolution of the unknown clustering amplitude $\mathrm{d}\beta_{\mathrm{u}}/\mathrm{d}z = 1$ instead of a constant evolution following R15. This tomographic sampling approach does not allow us to estimate $\beta_{\mathrm{u}}(z)$ using photo-z due to the thickness of the selected bins. This will be done in the colour sampling approach in Section 5.2.

We remind the reader that in this analysis, the photo-z information is only used to select subsamples localized in redshift in a pre-processing step. The only goal of photo-z here is to provide an easy way to select redshift distributions narrow in redshift but one can use any other way to do so. Once these subsamples are built, the only used information is the over/underdensity around reference galaxies which is used to estimate the redshift distribution. Then, cluster-z and photo-z methods could be used separately for validation and/or combined together.

4.3 Fainter unknown sample: 22.5 < i < 23

This section shows our ability to measure clustering redshifts when the unknown sample is fainter than the reference one.
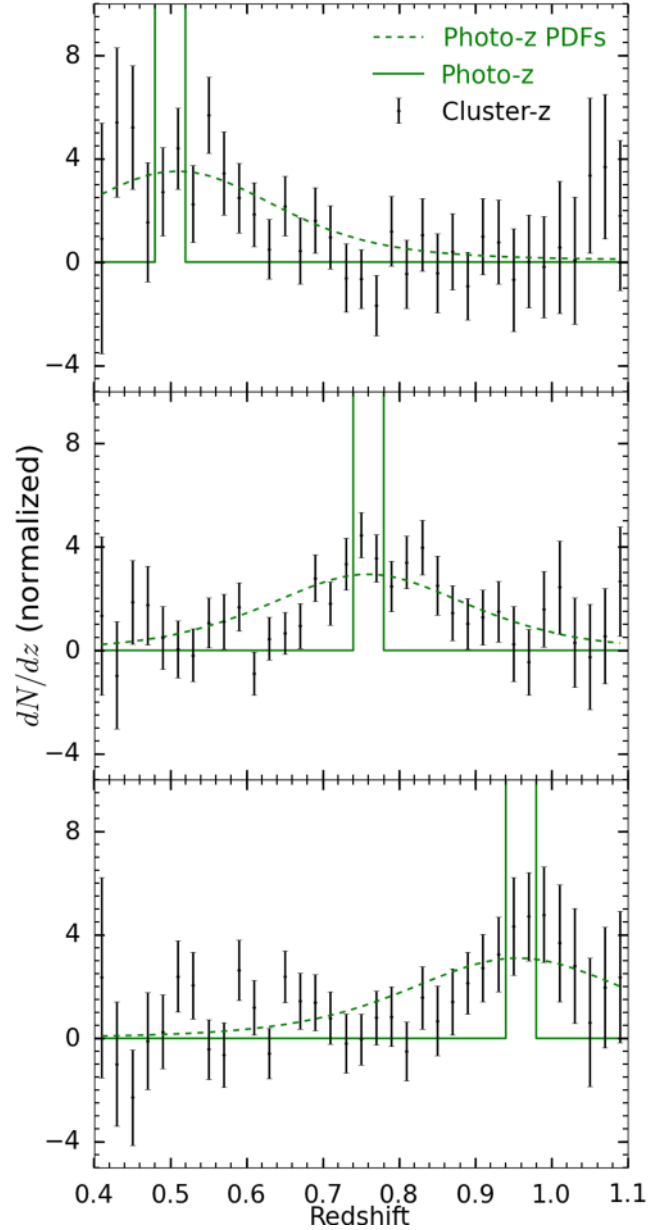

Figure 6. The cluster-z and photo-z distributions for several tomographic bins at magnitude $22.5 < i < 23$. Cluster-z (black points) are in agreement with photo-z PDFs (green dashed line) demonstrating that this method is able to extract the desired signal. The results for other bins are available online.

Table 1. Comparison between the mean clustering redshift and the mean photometric redshift from the distributions. This comparison is done when considering $\mathrm{d}\beta_{\mathrm{u}}/\mathrm{d}z = 0$ and $\mathrm{d}\beta_{\mathrm{u}}/\mathrm{d}z = 1$. In both cases, the two methods are in agreement.

| | $22.5 < i < 23$ | |
| | $\bar{z}_{\mathrm{clust}} - \bar{z}_{\mathrm{phot}}$ | |
	$\mathrm{d}\beta_{\mathrm{u}}/\mathrm{d}z = 0$	$\mathrm{d}\beta_{\mathrm{u}}/\mathrm{d}z = 1$
$\langle \Delta \bar{z} \rangle$	0.05	0.04
σ	0.06	0.06
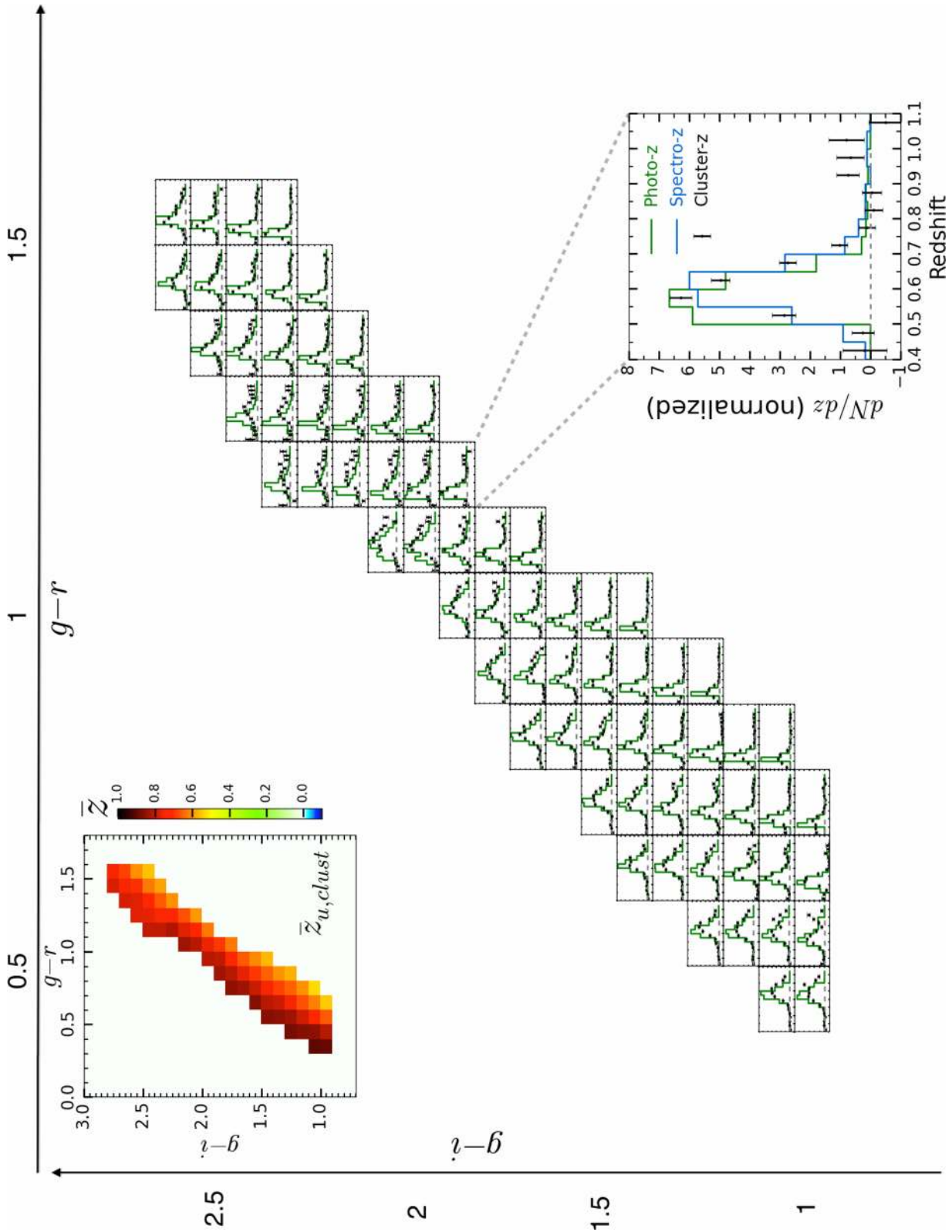
Figure 7. Cluster-z (black points) and photo-z distributions in each cell of the all colour-space for $i_{unk} < 22.5$. The top-left panel shows the evolution of the mean redshift with colours. A zoom for a given cell is shown in the bottom-right panel.
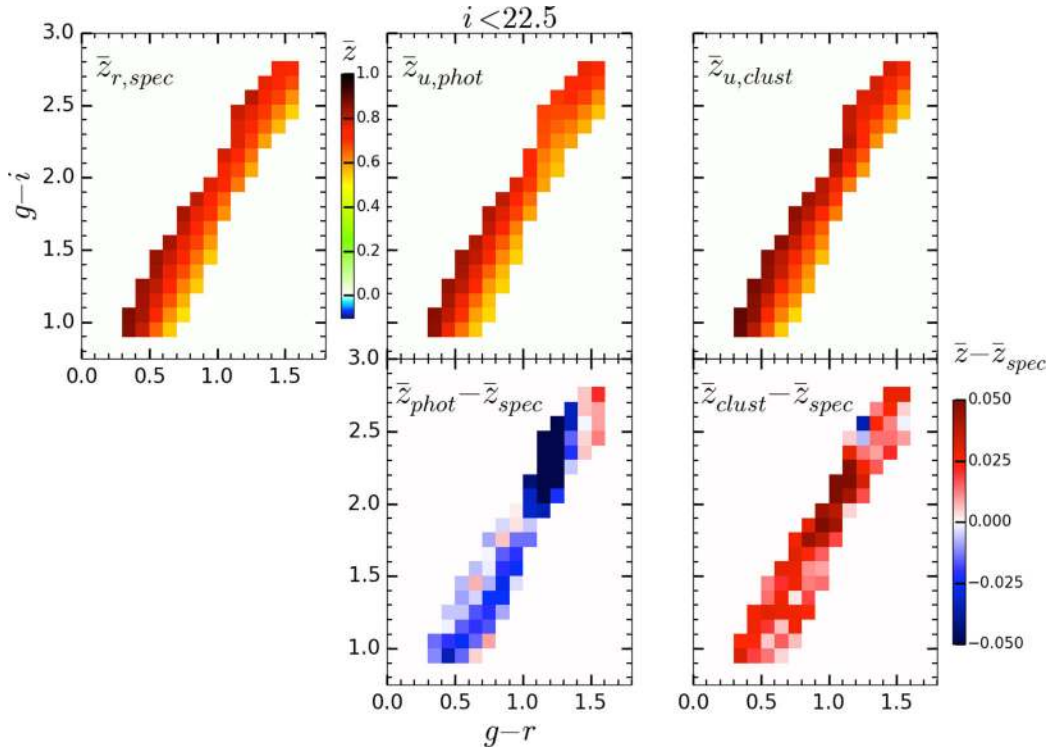
Figure 8. Top panel: mean redshift evolution through colour-space for both reference and unknown samples. Bottom panel: difference between the estimated mean redshift – cluster or photo-z – and the true mean redshift from spectroscopic measurements. One can notice a bad region around $g - r = 1.2$ for photo-z. This points out a systematic effect in the photo-z measurements.

Since we are not looking at the spectral energy distribution but at the clustering of objects and since all objects cluster with each other – regardless of their magnitude – we expect a signal (M13; Rahman et al. 2016a,b).

Nevertheless, since at a given redshift fainter objects are less massive, we can expect a lower signal than in the previous case. To illustrate this, we use the same reference population used previously with $i_{ref} < 22.5$ but we select objects from the unknown sample with $22.5 < i_{unk} < 23$. This leads to an unknown faint sample made of $N_u = 88\,000$ galaxies. To be coherent with the previous case, we build tomographic subsamples of $N_u = 3000$ galaxies.

The resulting clustering-based redshifts distributions for three selected bins that span the all redshift range are shown in black in Fig. 6. The measurements of all bins are available online. By computing the quantity $\bar{z}_{clust} - \bar{z}_{phot}$ for each distribution, one can estimate $\langle \Delta \bar{z} \rangle$ and the σ and then compare cluster-z to photo-z; see Table 1.

One can see that clustering-redshift distributions are in agreement with photo-z PDFs. Indeed, we find $\langle \Delta \bar{z} \rangle = 0.05$ and 0.04 and $\sigma = 0.06$ when considering $d\beta_u/dz = 0$ and $d\beta_u/dz = 1$, respectively. This demonstrates that the signal could be detected even when the reference and unknown populations do not have the same magnitude limit.

In the context of large imaging experiments, the requirements on spectroscopic redshifts are challenging. In particular, it is difficult to make complete spectroscopic samples down to magnitudes $i_{AB} = 24$ which is the magnitude limit of large imaging surveys like *Euclid*. This property of clustering redshift is therefore of great interest.

5 COLOUR SAMPLING

In this section, we aim at freeing the clustering-based redshift estimation technique from the need of photometric redshifts to pre-

select subsamples localized in redshift and quantify the resulting accuracy.

5.1 Magnitude limit for both samples: $i < 22.5$

First, we look at an unknown population with the same limiting magnitude of the reference sample. In this case, we expect the reference sample to be a representative sample of our unknown population. Then, the colour–redshift relation of both samples should be the same on average.

To reduce the effect of the clustering amplitude evolution with redshift of the unknown sample, $\beta_u(z)$, we build subsamples in colour-space. Working on the $(g - i; g - r)$ plane, we choose a binning size of $\Delta_{g-r/i} = 0.1$. By construction, the redshift distribution in each of these cells will be narrower than the one of the initial sample.

Then we measure the clustering redshift distribution in each cell. All these distributions across the colour-space as well as their corresponding photometric and spectroscopic redshift distributions can be seen in Fig. 7. The central part of this plot shows the redshift distribution evolution with colours.

When $g - r$ decreases, the redshift increases. This corresponds to the 4000 Å break going through the r band between redshift 0.4 and 1. On the contrary, $g - i$ increases with redshift. This is due to the 4000 Å break approaching the i band. The bottom-right panel is a zoom in one cell where one can see the clustering redshift distribution in black and the photo-z distribution in green. The top-left panel shows with a colour code the evolution of the mean clustering redshift with colours. This map gives a direct view of the colour–redshift relation reconstructed by clustering redshifts.

In the same way, the upper panels in Fig. 8 show the mean redshift evolution through colour-space but for both reference and unknown samples. This figure also shows in the bottom panels the differences:

Table 2. Comparison between the mean spectro/photo/cluster-z when considering $d\beta_u/dz = 0$. The bias and scatter of these two approaches are similar when comparing to spectroscopic redshift.

	$i < 22.5$	
	$\bar{z}_{phot} - \bar{z}_{spec}$	$\bar{z}_{clust} - \bar{z}_{spec}$
	$-$	$d\beta_u/dz = 0$
$\langle\Delta\bar{z}\rangle$	0.02	0.02
σ	0.04	0.03

$\bar{z}_{cl} - \bar{z}_{spec}$ and $\bar{z}_{ph} - \bar{z}_{spec}$. One can notice the large residuals for photo-z at $(g - i, g - r) \sim (2.2, 1.2)$. They reveal the presence of a systematic effect affecting the photo-z estimate. One can note that the template library has been calibrated with the CFHTLenS optical photometry whose absolute calibration differs by ~ 0.15 mag in the z band in comparison with the T0007 one (Moutard et al. 2016b). This could explain part of the photo-z bias that is observed for red galaxies. We leave to a future work a more detailed exploration of this effect.

To compare, in a more quantitative way, the ability of cluster-z to reproduce the colour–redshift relation compared to photo-z, we compte the residual $\bar{z}_{cl/ph} - \bar{z}_{spec}$ and summarize the results in Table 2. We find $\langle\Delta\bar{z}\rangle = 0.02$ for cluster-z and photo-z while they have $\sigma = 0.02$ and 0.03, respectively. This shows that in the colour sampling approach, cluster-z and photo-z have similar accuracy with respect to spectro-z. Nevertheless, one can note that here we use only

three bands to extract subsamples from the unknown population of objects. The resulting cluster-z are compared to photo-z while photo-z were obtained by combining optical and near-infrared data. This is encouraging because there is still plenty of information to be added. Other galaxy properties such as size, brightness and ellipticity can be used in addition to the colours to improve the cluster-z estimation.

5.2 Evolution of the unknown clustering amplitude $\beta_u(z)$

In this section, we investigate the validity of the assumption made on the evolution of the clustering amplitude of the unknown sample, $\beta_u(z)$.

Since we know the photometric redshifts for the unknown population, we can use them to estimate the true evolution with redshift of the clustering amplitude, $\beta_u(z)$. To do so, we apply the same procedure used in the measurement of the reference sample clustering amplitude, $\beta_r(z)$(see Section 3.1.3) following equation (8). This procedure is applied in each cell of the colour-space. Results are shown in Fig. 9 where we report the measured $\beta_u(z)$ based on photometric redshifts (in black), whereas in Fig. 2 and in the equations of Section 2, β is a function of $z_{spec} \sim z_{true}$. One can note that in these regions of the colour-space, the clustering amplitude $\beta_u(z)$ seems to evolve linearly with redshift. For this reason, we also show a linear fit (in green).

Based on these measurements, we can then compute the offset in the mean redshift, $\epsilon \equiv \bar{z}_{estimated} - \bar{z}_{true}$, due to the non-evolution hypothesis we made on the unknown clustering amplitude:
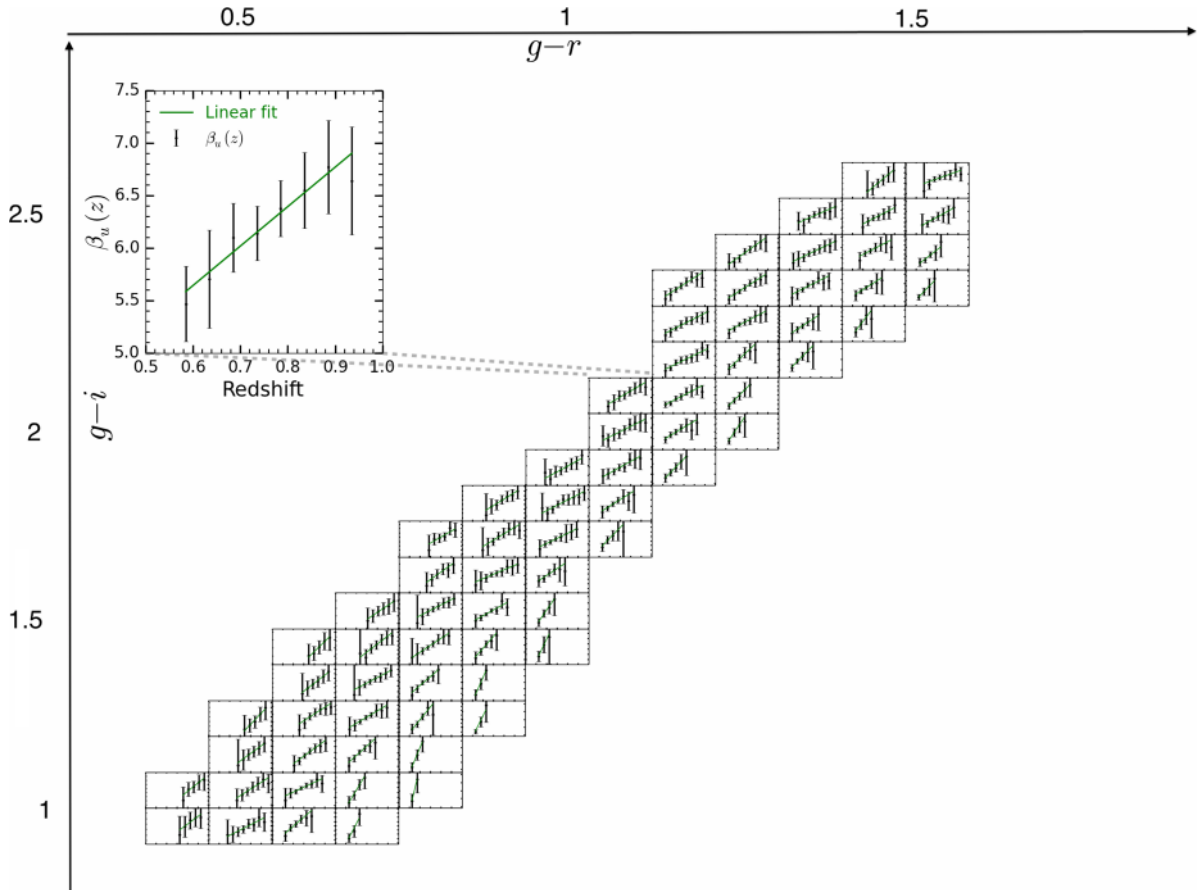
Figure 9. Black points show the measured clustering amplitude of the unknown sample $\beta_{u,true}(z)$ for each cell in the colour-space. The green line corresponds to a linear fit. This is computed using photo-z. A zoom for a given cell is shown in the top-right panel.
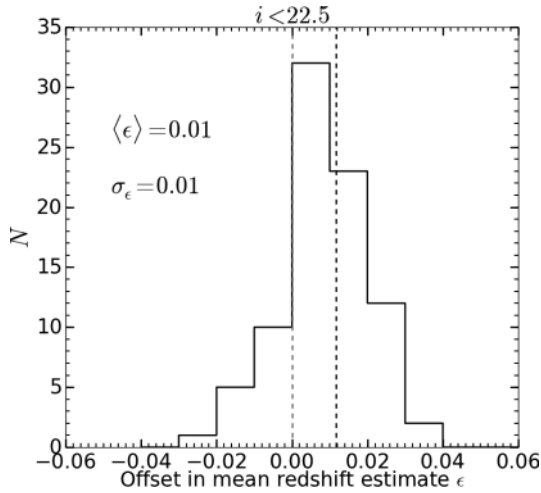
Figure 10. Offset in the mean redshift estimates due to the evolution of the unknown clustering amplitude $\beta_u(z)$. Considering no evolution for β_u leads to a bias of 0.02 in the mean redshift recovered by the clustering-based redshift estimation method.

Table 3. Same table than Table 2 but we add in grey the result when considering $d\beta_u/dz = 1$. This slightly improves the clustering redshift measurements.

	$i < 22.5$		
$\bar{z}_{phot} - \bar{z}_{spec}$		$\bar{z}_{clust} - \bar{z}_{spec}$	
–		$d\beta_u/dz = 0$	$d\beta_u/dz = 1$
$\langle \Delta\bar{z} \rangle$	0.02	0.02	0.01
σ	0.04	0.03	0.02

$d\beta_u/dz = 0$. The histogram showing the resulting offsets in the mean redshift estimates is visible in Fig. 10. In this case, the effect of considering $d\beta_u/dz = 0$ is a bias of the order of 0.02 in the mean redshift estimate.

Moreover, since the clustering amplitudes we measured seem to be linear in redshift, we can estimate the cluster-z distributions obtained in Section 5.1 when considering $d\beta_u/dz = 1$ in equation (9) instead of $d\beta_u/dz = 0$. The results of these new measurements are summarized in Table 3.

Finally, we combined all cluster-z measurements to derive the global redshift distribution in Fig. 11. The top panel shows the two photo-z distributions as well as the global clustering redshift distributions when accounting or not for a linear evolution of $\beta_u(z)$. These distributions are obtained by summing the distributions from each cells in colour-space including cells located in the bad region of the photo-z map(see Fig. 8). Considering a linear evolution for $\beta_u(z)$ allows us to correct the small distortion of the distribution. As expected, it appears that the no-evolution assumption tends to slightly underestimate the number of galaxies at low redshift and to slightly overestimate it at high redshift.

The bottom panel of Fig. 11 shows the same quantities but when summing the distributions only from the 'good' cells in colour-space. In this case, we excluded cells located in the bad region of the photo-z map, i.e. cell in the two columns at $g - r \sim 1.2$.

5.3 Fainter unknown sample: $22.5 < i < 23$

In this section, we apply the same sampling approach in colour-space as previously but we use the fainter unknown sample defined in Section 4.3 with $22.5 < i_{unk} < 23$.
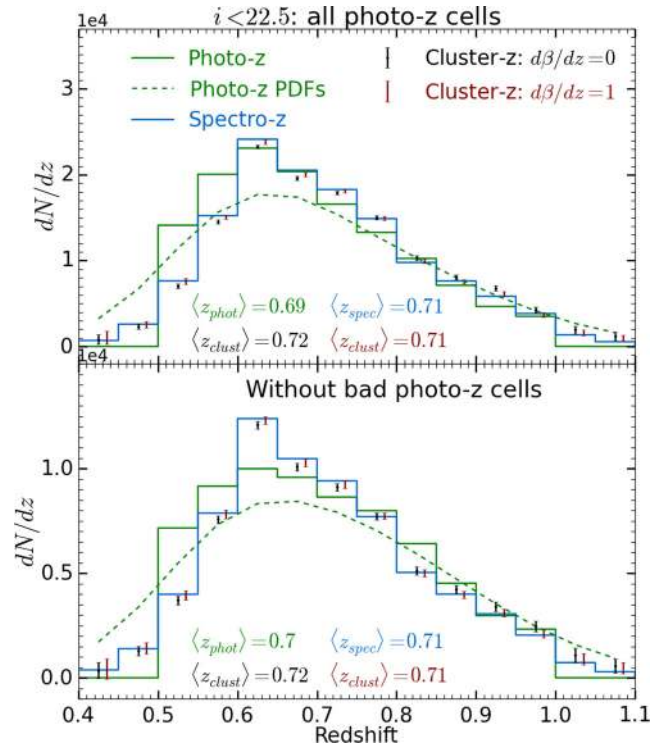
Figure 11. Top panel: global redshift distribution estimated by photo-z (green and dashed green), spectro-z (blue) and by cluster-z (black dots) for $d\beta_u/dz = 0$. Red dots correspond to cluster-z with $d\beta_u/dz = 1$. These distributions are obtained by adding the distributions of the all cells of the colour-space, including the bad region visible in Fig. 8. Bottom panel: as the top panel but excluding cells in the two columns around $g - r \sim 1.2$.

This time the colour–redshift relation of both samples are not supposed to be the same. To check our results, we then used VVDS data (Le Fèvre et al. 2005, 2013) for which we corrected the magnitudes to be calibrated in the same way than the CFHTLS data.

The VVDS data are then selected to have $22.5 < i < 23$ leading to a complete sample of ~ 1000 sources. Since this sample is very small and cover an area smaller than VIPERS, one can only expect to have agreement on averaged statistical properties due to cosmic variance.

Then we computed the corresponding clustering redshift distributions visible in Fig. 12. Those distributions were computed by considering $d\beta_u/dz = 1$.

Fig. 13 shows the resulting colour–redshift map in the top panels. The corresponding residuals for the faint colour sampling analysis are in the bottom panels. Due to the low number of spectroscopic sources, the residuals are all within the stochastic noise of the mean redshift estimate which can be estimated to be ~ 0.1. The summary statistics of these measurements are shown in Table 4.

In the top panel, we found $\langle \Delta\bar{z} \rangle = 0.03$ and $\sigma = 0.05$ for photo-z and $\langle \Delta\bar{z} \rangle = 0.05$ and $\sigma = 0.07$ for cluster-z when considering no evolution with redshift for β_u, while we found $\langle \Delta\bar{z} \rangle = 0.04$ and $\sigma = 0.06$ when considering $d\beta_u/dz = 1$, in the bottom panel. In both cases, the cluster-z and photo-z measurements are in agreement.

Finally, we combine all distributions from Fig. 12 and reconstruct the global clustering redshift distribution of the fainter unknown population (see Fig. 14). As we could expect, we found results in good agreement between photo-z and cluster-z.

Fig. 14 shows that in the colour-sampling approach, cluster-z and photo-z distributions are similar when the unknown sample is
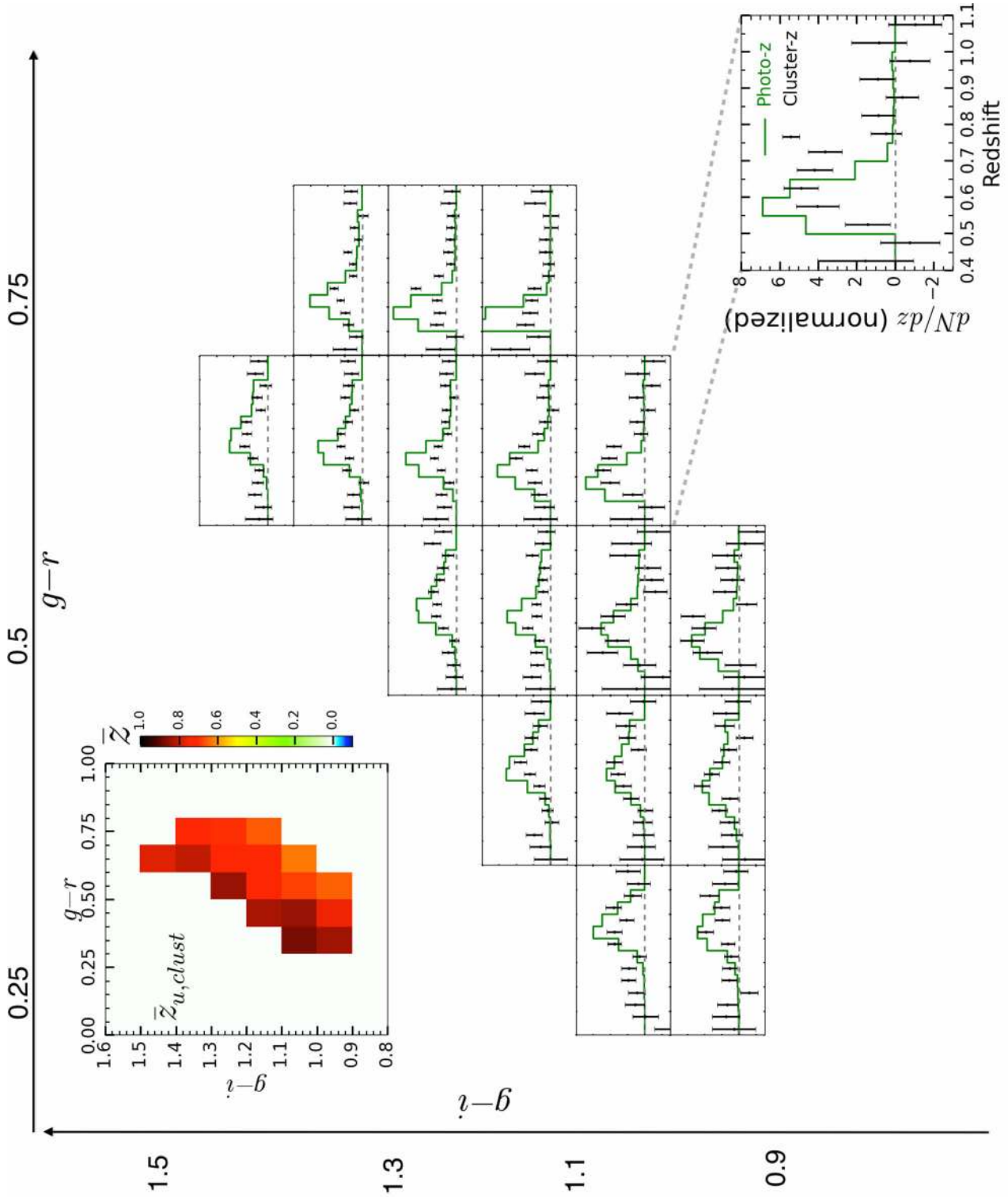
Figure 12. Cluster-z (black points) and photo-z distributions in each cell of the all colour-space for $22.5 < i_{unk} < 23$. The top-left panel shows the evolution of the mean redshift with colours. A zoom for a given cell is shown in the bottom-right panel.
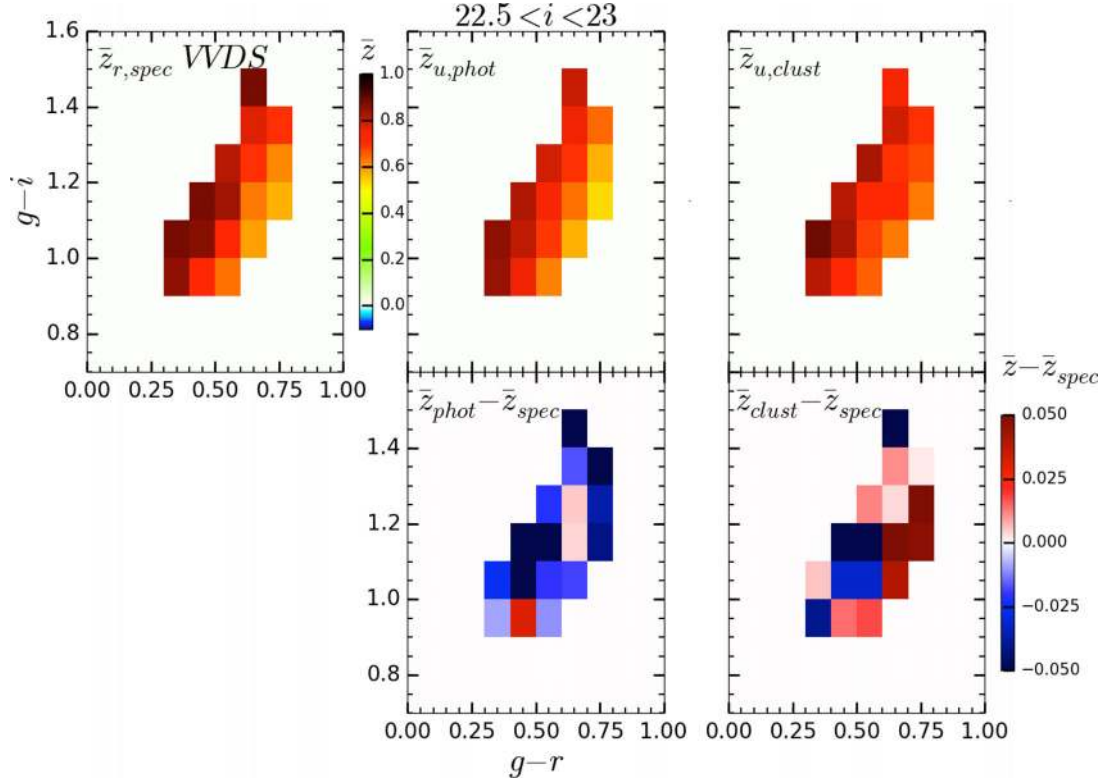
Figure 13. Top: mean redshift evolution through colour-space for the unknown sample and for spectroscopic data from VVDS. Bot: difference between the estimated mean redshift – cluster or photo-z – and the true mean redshift from VVDS spectroscopic measurement. The residuals are all within the stochastic noise of the mean redshift estimate.

Table 4. Same table than Table 3 but we add in grey the results when considering $d\beta_u/dz = 0$ and $d\beta_u/dz = 1$ in the case where the unknown population is fainter than the reference sample.

| | | $i < 22.5$ | | | $22.5 < i < 23$ | |
| | $\bar{z}_{phot} - \bar{z}_{spec}$ | $\bar{z}_{clust} - \bar{z}_{spec}$ | | $\bar{z}_{phot} - \bar{z}_{spec}$ | $\bar{z}_{clust} - \bar{z}_{spec}$ | |
	−	$d\beta_u/dz = 0$	$d\beta_u/dz = 1$	−	$d\beta_u/dz = 0$	$d\beta_u/dz = 1$
$\langle \Delta\bar{z} \rangle$	0.02	0.02	0.01	0.03	0.05	0.04
σ	0.04	0.03	0.02	0.05	0.07	0.06
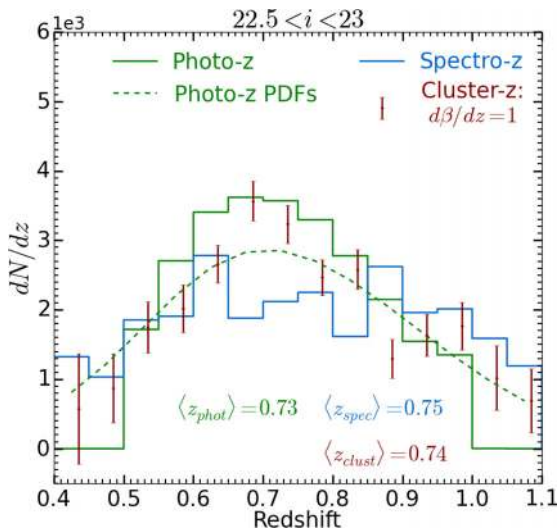
Figure 14. Comparison between the global redshift distributions of the unknown sample measured by cluster-z with $d\beta_u/dz = 1$ (red points), photo-z (green line), spectro-z from VVDS (blue line).

fainter than the population of reference. As said previously, it is difficult to make faint complete spectroscopic samples. This property of clustering redshifts could be of great interest. Moreover, we remind the reader that we use only three bands to subsample the unknown population, whereas photo-z were obtained by combining optical and near-infrared data. We also remind that the spectroscopic distribution visible in blue is not the exact solution since it is a very small sample. Only averaged quantities should be compared.

6 SUMMARY

We have explored and quantified the ability of clustering-based redshift using VIPERS and CFHTLS. The method adopted in this paper follows the one presented in M13.

(i) We demonstrated our ability to measure the clustering redshift distribution using a tomographic photo-z sampling. We found similar accuracy between photo-z and cluster-z.

(ii) We investigated the potential of this method to estimate redshift distributions of samples fainter than the magnitude limit of the reference population. In this case, we also shown that the cluster-z

accuracy is similar to photometric redshift. This suggest that the reference sample do not need to be representative of the unknown sample. This property could be of great interest to estimate redshifts in the context of future large surveys.

(iii) We have removed cluster-z from requirement of photo-z by selecting subsamples in colour-space. This allows the cluster-z measurement to be independent of the photometric redshift. That means that cluster-z does not suffer from possible systematics due to the photo-z procedure. Both methods could then be used to validate the other one. One could also try to combined them together.

(iv) We used the last two points to explore the ability of the clustering-based redshift estimation method to probe the redshift distribution of a sample in a magnitude range fainter than and non-overlapping with the reference population, independently of photometric redshift. As said previously, such property could be of great interest in the context of future large imaging surveys, like the *Euclid space mission*.

It is important to notice that in some case, e.g. for a galaxy population with strong scale-dependent bias, the local approach could not be sufficient. This would lead to a biased estimate of the redshift distribution. Since the galaxy bias is a strictly increasing function with redshift (Fry 1996; Tegmark & Peebles 1998), this would induce an under/overestimation of the cluster-z distribution at low/high redshift. Also cosmic variance can affect these results in particular in Section 5.3 when comparing cluster-z to VVDS spectroscopic data.

In future works, we will study in more detail within simulations the accuracy reachable using this method in the context of *Euclid*. We will also investigate the number of reference objects and number of filters needed to reach the *Euclid* photo-z requirements, alone and/or when combined with photo-z. Also, the clustering properties of galaxies beyond $z = 1$ could affect the measurement. This will be explored in future works. It is important to realize that the performance of this approach will keep increasing, mostly because of the increase of the spectroscopic data. Indeed, for a given unknown population, the statistical noise will decrease with each new spectroscopic redshift, and also because there is still plenty of information to be added to break the colour-redshift degeneracy. For example, one can add other kind of information such as size, brightness, ellipticity. These points will also be explored in a future work.

ACKNOWLEDGEMENTS

REFERENCES

Albrecht A. et al., 2006, preprint (arXiv:astro-ph/0609591)
Amendola L. et al., 2013, Liv. Rev. Relativ., 16, 6
Bernstein G., Huterer D., 2010, MNRAS, 401, 1399
Coleman G. D. et al., 1980, ApJS, 43, 393
Connolly A. J. et al., 1995, AJ, 110, 2655
Cooper M. C. et al., 2006, MNRAS, 370, 198
Davis M., Peebles P. J. E., 1983, ApJ, 267, 465
Fry J. N., 1996, ApJ, 461, L65
Guzzo L. et al., 2014, A&A, 566, A108
Hearin A. P. et al., 2010, ApJ, 720, 1351

Huterer D. et al., 2006, MNRAS, 366, 101

Knox L., Song Y.-S., Zhan H., 2006, ApJ, 652, 857

Landy S. D., Szalay A. S., Koo D. C., 1996, ApJ, 460, 94

Laureijs R. et al., 2011, preprint (arXiv:1110.3193)

Le Fèvre O. et al., 2005, A&A, 439, 845

Le Fèvre O. et al., 2013, A&A, 559, A14

McQuinn M., White M., 2013, MNRAS, 433, 2857

Ma Z., Hu W., Huterer D., 2006, ApJ, 636, 21

Marulli F. et al., 2013, A&A, 557, A17

Matthews D. J., Newman J. A., 2010, ApJ, 721, 456

Matthews D. J., Newman J. A., 2012, ApJ, 745, 180

Ménard B., Scranton R., Schmidt S., Morrison C., Jeong D., Budavari T.,
    Rahman M., 2013, preprint (arXiv:1303.4722) (M13)

Moutard T. et al., 2016a, A&A, 590, A102

Moutard T. et al., 2016b, A&A, 590, A103

Newman J. A., 2008, ApJ, 684, 88

Newman J. et al., 2015, ApJ, 63, 81

Phillipps S., Shanks T., 1987, MNRAS, 229, 621

Rahman M., Ménard B., Scranton R., Schmidt S. J., Morrison C. B., 2015,
    MNRAS, 447, 3500 (R15)

Rahman M., Ménard B., Scranton R., 2016a, MNRAS, 457, 3912

Rahman M., Mendez A. J., Ménard B., Scranton R., Schmidt S. J., Morrison
    C. B., Budavàri T., 2016b, MNRAS, 460, 163

Schmidt S. J. et al., 2013, MNRAS, 431, 3307

Schmidt S. J. et al., 2015, MNRAS, 446, 2696

Seldner M., Peebles P. J. E., 1979, ApJ, 227, 30

Sun L. et al., 2009, ApJ, 699, 958

Tegmark M., Peebles P. J. E., 1998, ApJ, 500, L79

Thomas S. A. et al., 2011, MNRAS, 412, 1669

Zhan H., 2006, J. Cosmol. Astropart. Phys., 8, 8

Zhan H., Knox L., 2006, ApJ, 644, 663

SUPPORTING INFORMATION

Additional Supporting Information may be found in the online version of this article:

**Scoltez_Clustering_redshift_Paper.tar
supplementary_online_material.tar**
(http://www.mnras.oxfordjournals.org/lookup/suppl/doi:10.1093/mnras/stw1500/-/DC1).

Please note: Oxford University Press is not responsible for the content or functionality of any supporting materials supplied by the authors. Any queries (other than missing material) should be directed to the corresponding author for the article.

This paper has been typeset from a TEX/LATEX file prepared by the author.